Nanoscale

PAPER

View Article Online
View Journal | View Issue

Cite this: *Nanoscale*, 2025, **17**, 4578

Dextran stabilised hematite: a sustainable anode in aqueous electrolytes†

Sofia Panagiotidou,‡[a] Evangelia Vasilaki, *‡§[a,b] Nikos Katsarakis,[c] Dimitra Vernardou *[c] and Maria Vamvakaki[a,b]

During the last decades, the use of innovative hybrid materials in energy storage devices has led to notable advances in the field. However, further enhancement of their electrochemical performance faces significant challenges nowadays, imposed by the materials used in the electrodes and the electrolyte. Such problems include the high solubility of both the organic and the inorganic anode components in the electrolyte as well as the limited intrinsic electronic conductivity and substantial volume variation of the materials during cycling. The present work focuses on the fabrication of novel and sustainable anode electrodes for use in energy storage devices, utilizing cross-linked oxidized dextran (Ox-Dex) as the binder and hematite (α-Fe_2O_3) cubes as the active component. The ion diffusion mechanism within the anode electrode materials, as well as their cycling stability, were studied *via* cyclic voltammetry measurements, using Li^+, Zn^{2+} and Al^{3+} aqueous electrolytes. The hybrid iron oxide electrodes exhibited the highest electrochemical performance in the $Al_2(SO_4)_3$ electrolyte (3000 mA g^{-1}), followed by $ZnSO_4$ (2000 mA g^{-1}) and Li_2SO_4 (800 mA g^{-1}). The differences in the performance of the anodes for the three investigated electrolytes were attributed to the ionic radii of Li^+, Zn^{2+} and Al^{3+}, which affect the rate of ion diffusion within the material lattice exhibiting the highest diffusion coefficient of 4.64×10^{-9} cm^2 s^{-1} in Al^{3+}. Notably, the hybrid anodes demonstrated superior cycling performance (with the lowest variance percentage of 1.3% for hybrid compared to 38.1% for the bare in the presence of Zn^{2+}), underlining the pivotal role of the natural binder. This was attributed to hydrogen bonding interactions, which increase the contact points between the inorganic and polymeric components, resulting in a more uniform network structure. Additionally, the cross-linking of Ox-Dex promotes stability and tolerance to the volume expansion of the electrodes. These results underscore the immense potential of the proposed hybrid electrodes in the field of energy storage.

Received 21st November 2024,
Accepted 7th January 2025

DOI: 10.1039/d4nr04897k

rsc.li/nanoscale

1. Introduction

The increasing energy storage demands in modern society have brought to light certain limitations of lithium-ion batteries (LIBs), including their non-effective delivery of large amounts of power, high cost and poor safety.[1,2] From this perspective, alternative battery chemistries, such as those based on Zn^{2+} and Al^{3+} multivalent ions, have appeared as attractive options.[3] Zinc ion batteries (ZIBs) are of great interest, due to their low cost, environmental friendliness, acceptable energy density (80–150 W h kg^{-1})[4] suitable for stationary and low-power applications and safety in mild aqueous electrolytes.[5] The electrochemical dissolution and deposition of zinc takes place at ~0 V *vs.* Zn^{2+}/Zn, which renders the process ideal for the anodic reaction.[6] In addition, ZIBs benefit from the high ionic conductivity of Zn^{2+} (1.57×10^{-3} S cm^{-1}), achieving a much faster charge/discharge rate compared to Li^+ (10^{-6} S cm^{-1}),[7] and the higher abundance of the element in the Earth's crust compared to Li.[8] On the other hand, Al^{3+} stands out as a trivalent cation, being the most prevalent metal in the Earth's crust (8.1%).[9] Aluminum also possesses enhanced ion diffusion and achieves improved electrochemical behavior, due to its relatively small ionic radius (R = 53.5 pm) compared to other metal ions (Zn^{2+}: 74 pm and Li^+: 76 pm).[8,10–12] Finally, aluminum ion batteries are highly recyclable, and therefore more sustainable, compared to LIBs.[10] While, multivalent ion

[a]*Department of Materials Science and Engineering, University of Crete, 700 13 Heraklion, Crete, Greece. E-mail: evasilaki@iesl.forth.gr*
[b]*Institute of Electronic Structure and Laser, Foundation for Research and Technology – Hellas, 700 13 Heraklion, Crete, Greece*
[c]*Department of Electrical & Computer Engineering, School of Engineering, Hellenic Mediterranean University, Heraklion, 710 04 Crete, Greece.*
E-mail: dvernardou@hmu.gr

†Electronic supplementary information (ESI) available. See DOI: https://doi.org/10.1039/d4nr04897k

‡These authors contributed equally.

§Current affiliation: Max-Planck Institute of Colloids and Interfaces, Department of Colloid Chemistry, Am Mühlenberg 1, 14476 Potsdam, Germany.

batteries hold great promise, the search for suitable anode materials compatible with these electrolytes presents significant challenges. These materials encounter similar issues to lithium, particularly regarding dendrite formation and electrode volume changes.[13] Zinc anodes in particular, are prone to corrosion, which can diminish the battery lifespan and performance,[14] while aluminum foil anodes, undergo drastic structural degradation induced by the large volume changes during the battery reactions.[15] This discrepancy occurs due to aluminum's ability to form a stable, protective oxide layer on its surface, which serves as a barrier that shields the underlying metal from further oxidation or reaction with the environment.

To address these challenges, hybrid nanostructured materials that combine active materials with organic binders have been intensively studied as potential anode materials, as they offer improved performance, lower degradation, superior safety and enhanced versatility compared to the single component systems.[16–19] Various materials have been evaluated for their applicability as the active components in anode electrodes, including carbon-based materials, tin alloys, antimony and phosphorus.[20–22] Transition metal oxides have been also explored in hybrid materials development, for electrode fabrication, due to their high electrochemical performance, capacity reversibility during the ion charging/discharging processes and straight-forward synthetic routes.[23–25] Among them, hematite, Fe_2O_3, stands out as a highly promising candidate, owing to its remarkable attributes that include high theoretical capacity (1007 mA h g^{-1}), stability at ambient conditions, natural abundance, low cost, and environmentally friendly nature.[26–28] The organic binder constitutes the second key component in hybrid anode electrodes, as it has been recognized to affect the aging, irreversible capacity loss and coulombic efficiency of the battery.[29] The most widely studied binders refer to conventional synthetic polymers, mainly polyvinylidene fluoride (PVDF), but also polyacrylic acid and its sodium or lithium salts, polyimide, polyvinylpyrrolidone, polyacrylonitrile and polyvinyl alcohol.[30–34] However, growing environmental concerns on synthetic polymers have lately shifted the attention to natural and aqueous-based binders as greener alternatives. Polysaccharides, such as carboxymethyl cellulose, chitosan, gum arabic and alginates, are attractive candidates, due to their affordability, water solubility and environmentally friendly nature.[30,33,35–37] Moreover, these natural polymers possess numerous functional groups that can interact with the active material, or be exploited in cross-linking reactions towards the formation of hyperbranched networks. As a result, hybrid electrodes with excellent mechanical properties are fabricated, capable of buffering the volume fluctuations that occur during battery cycling, which lead in irreversible slipping of the active material and structural fractures between the active particles, and eventually in poor battery stability.[38–40]

In contrast to the aforementioned polysaccharides, dextran, a water-soluble, natural glucan, rich in hydroxyl groups, has received negligible attention. Recently, hybrid anode electrodes combining silicon and graphite materials with dextran were reported to exhibit high coulombic efficiency and good cycling in Li-ion cells, a performance that was found superior to the conventional PVDF and poly(acrylic acid sodium salt) binder.[41] In another interesting work, a modified analogue of dextran, lithium dextran sulfate, was used as a protective binder in Li-ion batteries. The lithiated polysaccharide was found to dynamically bind onto both a Cu foil current collector and metallic Li, through its chemically introduced –O-SO_3– functional groups, preventing the formation of dendrites and stabilizing the electrode interface, again surpassing the inferior stability of the conventional PVDF binder.[42] Nevertheless, in all these reports non-aqueous, carbonate-based electrolytes were employed, which should be replaced with aqueous analogues towards more advanced, green and sustainable energy storage systems of lower cost and higher safety.[43] This future prospect, however, limits the applicability of natural, hydrophilic polymers, because they are soluble in the aqueous battery electrolytes, a characteristic which deteriorates the stability and performance of the electrode *via* the dissolution of the binder and the loss of the active material in the electrolyte.[31]

In the present study, we aim to develop and evaluate high performance and environmentally friendly hybrid anode electrodes in aqueous metal ion electrolytes. Oxidized dextran (Ox-Dex), a chemically modified analogue of the natural polysacharide, was employed as the polymeric binder to immobilize hematite pseudocube particles as the active material. The cross-linking of Ox-Dex *via* hydrazone bonds, served the essential purpose of preventing the dissolution of the binder and thus the loss of the active material in the aqueous electrolyte, while more importantly it ensured the structural integrity of the hybrid electrode during the intercalation/de-intercalation processes due to the elasticity of the polymer and the dynamic nature of the hydrazone bonds. The performance and stability of the hybrid electrodes were also promoted by hydrogen bonding interactions, which can be reversibly disrupted and reformed during cycling, between the remaining, non-oxidized hydroxyl groups of the natural polymer and the surface functionalities of the hematite particles. A holistically green, water-based approach was employed during all steps, from the synthesis or chemical modification of the precursors, the electrode fabrication and electrochemical evaluation of the anodes. Lithium sulfate ($Li_2(SO_4)$), zinc sulfate ($ZnSO_4$) and aluminum sulfate ($Al_2(SO_4)_3$) were employed as sustainable aqueous electrolytes, while the diffusion mechanism of the Li^+, Zn^{2+}, and Al^{3+} ions within the hybrid material lattice was elucidated by cyclic voltammetry measurements, performed at various scan numbers and rates. The stability of the prepared hybrid anodes was also verified *via* physicochemical and morphological analyses in Zn^{2+}. These analyses highlighted their promising electrochemical performance in terms of stability and diffusion coefficient, compared to values reported in the literature for the specific chemistry. Moreover, the results affirmed the preservation of their morphology and structure after continuous intercalation/de-intercalation cycles.

2. Materials and methods

2.1 Materials

Dextran T-40 (MW = 40 kDa) was purchased from Serva. Methyl orange (dye content 85%) was supplied from Fluka. Sodium metaperiodate (ACS reagent, 99%), hydroxylamine hydrochloride (ACS reagent, 98%), ferric chloride anhydrous (ACS reagent, 99.9%), sodium sulfate anhydrous (ACS reagent, ≥99%), sodium hydroxide anhydrous (ACS reagent grade, ≥98%, pellets), adipic acid dihydrazide (AAD) (≥98%), lithium sulfate (≥98%), aluminum sulfate hydrate (97%) and zinc sulfate heptahydrate (98%) were supplied from Sigma-Aldrich. All chemicals were used as received. Milli–Q water with a resistivity of 18.2 MΩ cm at 298 K was obtained from a Millipore apparatus and was used for all experiments.

2.2 Synthesis of the α-Fe_2O_3 particles

α-Fe_2O_3 particles were synthesized using a protocol reported by Sugimoto *et al.*[44] In specific, 100 mL of a 2 M $FeCl_3$ solution were added to 90 mL of a 6 M NaOH solution under stirring. Next, the solution was transferred into a sealed Pyrex bottle and was placed in an oven thermostated at 100 °C, and was allowed to age for 8 d. The red product was collected by filtration, washed three times with ethanol and Milli–Q water, followed by drying overnight under vacuum.

2.3 Oxidation of dextran (Ox-Dex)

The oxidation of dextran was carried out targeting a 30% degree of oxidation, taking into account that the quantitative oxidation of the dextran hydroxyl groups requires a 2 : 1 molar ratio of $NaIO_4$ over the saccharide repeat units.[45] Briefly, dextran (3.56 g, 0.022 moles) was first dissolved *via* stirring in 400 mL Milli–Q water. Then, 2.78 g $NaIO_4$ (0.013 moles) were added to the dextran solution and the reaction vessel was wrapped with an aluminum foil and was left under stirring at room temperature overnight. Finally, the product was purified by dialysis against water using a dialysis membrane with a cut-off limit of 3500 Da. Finally, the aqueous Ox-Dex solution was lyophilized to afford the product as a white solid.

2.4 Preparation of the bare α-Fe_2O_3 electrodes

For the fabrication of the electrodes of ~400 μm thickness, a conventional drop casting technique on Cu substrates with a surface area of 2.25 cm^2, was employed. On each substrate, 0.35 g of a 4 wt% aqueous dispersion of the α-Fe_2O_3 particles, corresponding to ~0.014 g active material, were drop-casted using a micropipette. The electrodes were dried under vacuum at room temperature until the complete evaporation of the solvent.

2.5 Preparation of the hybrid α-Fe_2O_3/Ox-Dex electrodes

For the fabrication of the hybrid α-Fe_2O_3/Ox-Dex electrodes, 0.35 g of a 0.8 wt% aqueous solution of Ox-Dex was prepared, followed by the addition of 0.014 g α-Fe_2O_3, targeting a 5 : 1 mass ratio of inorganic particles to the polymer binder. Next, 2.1 μL of a 100 mg mL^{-1} AAD cross-linker solution were added in the α-Fe_2O_3/Ox-Dex solution under continuous stirring. Finally, the suspension was uniformly deposited onto a Cu substrate, with a surface area of 2.25 cm^2, by drop casting and was dried under vacuum at room temperature to prepare hybrid electrodes with a comparable film thickness to the bare analogues.

2.6 Characterization methods

2.6.1 Determination of the degree of oxidation of dextran. To determine the degree of oxidation of dextran, a 0.25 M aqueous solution of hydroxylamine hydrochloride was first prepared.[46] Then, 6 ml of a 0.05% w/v aqueous solution of methyl orange were added, followed by dilution to a total volume of 1 L with Milli–Q water. The solution was left under stirring overnight wrapped in an aluminum foil. Next, 0.1 g Ox-Dex were dissolved in 25 ml of the hydroxylamine hydrochloride/dye solution under stirring overnight in the dark. Finally, the titration curve of Ox-Dex was obtained by monitoring the pH changes in the polymer solution, upon addition of aliquots of 0.1 M NaOH, using a Sen-Tix 81 pH electrode. The equivalent point was also observed optically by monitoring the color change of the polymer solution from light red to orange, which corresponded to the color of the control sample *i.e.* in the absence of the oxidized polymer.

2.6.2 Physicochemical and morphological characterization. The crystal structure of the samples was determined by X-ray diffraction (XRD) using a Panalytical Expert Pro X-ray diffractometer with a CuKα X-ray radiation (λ = 1.5406 Å), while their surface morphology and elemental analysis (EDS) was studied by FE-SEM (JEOL JSM-7000F). Samples were prepared by drop casting the polymer/hydrid material solutions on glass slides and allowing them to dry overnight at room temperature. Each sample was sputter-coated with 10 nm of Au before imaging. Finally, the wettability of the electrodes was evaluated *via* contact angle measurements using an OCA-35 contact angle measuring set-up from Dataphysics, with a SCA-20 software. The contact angle measurements were performed in triplicates using 4 μL droplets of the aqueous solutions.

2.7 Electrochemical experiments

The electrochemical performance of the samples was evaluated using an electrochemical cell with a typical tri-electrode configuration and a computer-controlled AUTOLAB potentiostat/galvanostat.[47,48] Ag/AgCl and graphite were used as the reference and the counter electrodes, respectively, whereas the material under investigation was used as the working electrode, with a geometric area of 2.25 cm^2, in each case. Aqueous solutions of 1 M Li_2SO_4, $ZnSO_4{\cdot}7H_2O$ and $Al_2(SO_4)_3{\cdot}H_2O$ were employed as the electrolytes, and the scan rate was kept constant at 20 mV s^{-1} for all electrolytes. The operating potential window for Li_2SO_4 was −0.75 to +0.1 V, for $ZnSO_4$ −0.65 to +0.15 V and for $Al_2(SO_4)_3$ −0.55 V to +0.25 V. Cyclic voltammograms were also obtained at scan rates of 5, 10, 20, 30, 40, 50 and 100 mV s^{-1} to elucidate the metal ion intercalation mechanism and estimate the diffusion coefficient of each metal. The current was expressed as specific current (A

g^{-1}) relative to the mass of the electrode material that was immersed in the electrolyte. All electrochemical tests were carried out at room temperature (25 °C).

3. Results and discussion

3.1 Physicochemical and morphological characterization of Ox-Dex and of the α-Fe_2O_3 particles

The oxidation of dextran proceeded under mild aqueous conditions using sodium periodate as the oxidizing agent. The targeted degree of oxidation was 30% based on previous studies in our lab, which showed that at this degree of modification the polymer presented sufficient aldehyde groups that allowed its effective cross-linking to form a stable gel. Moreover, an adequate number of hydroxyl groups was also left intact to facilitate the favorable interactions between the oxidized polysaccharide and the inorganic particle surface. The experimental degree of oxidation of dextran was determined *via* the reaction of the newly formed aldehyde groups with hydroxylamine hydrochloride to obtain oxime moieties. The simultaneous release of hydrochloric acid was both potentiometrically and colorimetrically titrated using a standard 0.1 M sodium hydroxide solution (see Fig. S1†). The percentage of aldehyde groups was calculated 33% using equation S1, in good agreement with the theoretical value.

Iron oxide particles were prepared using a simple and straight-forward sol–gel approach in water. The morphology of the α-Fe_2O_3 particles was studied *via* FE-SEM, and a characteristic cube-like morphology with an average size of ~1.5 ± 0.2 μm was observed (Fig. S2a†). The growth process of hematite pseudocubes proceeds *via* a multi-step process.[49] First, Fe^{3+} is hydrolyzed *via* the addition of the alkaline solution in the gel–sol system, resulting in the precipitation of β-FeOOH in the form of rods, along with the formation of small hematite nuclei. Finally, hematite cube-like particles are formed *via* the dissolution of ferric species from the akaganéite rods and their recrystallization on the growing hematite nuclei. The shape of the hematite cubes is dictated by the adsorption of the chloride anions onto the (012) face of the crystals, restraining their growth in the direction normal to this face. Moreover, the crystallinity and purity of the as-prepared particles were investigated *via* XRD and the respective pattern indicated a pure phase of rhombohedral α-Fe_2O_3 (see Fig. S2b†) with a crystallite size of ~29 nm quantified by the Scherrer equation (eqn (S2)†). In specific, the characteristic diffraction peaks at 24°, 33°, 35°, 40°, 49°, 54°, 62° and 64° were assigned to the (012), (104), (110), (113), (024), (116), (214) and (300) planes of α-Fe_2O_3, respectively.[50] No secondary phases or impurities were detected, signifying the high purity of the obtained hematite nanoparticles.

3.2 Physicochemical and morphological characterization of the bare α-Fe_2O_3 and hybrid α-Fe_2O_3/Ox-Dex electrodes

Bare α-Fe_2O_3 electrodes were prepared by drop casting aqueous dispersions of the hematite particles on Cu substrates. The hybrid α-Fe_2O_3/Ox-Dex analogues were fabricated *via* the deposition of a mixture of Ox-Dex and hematite particles at a 1 : 5 mass ratio, following a protocol reported in the literature.[41] To ensure the stability of the hybrid coating, the aldehyde groups of Ox-Dex were cross-linked using AAD as a bifunctional cross-linker to form hydrazone bonds. The crystallinity and morphology of the bare α-Fe_2O_3 and the hybrid α-Fe_2O_3/Ox-Dex electrodes were investigated *via* XRD and FE-SEM measurements, respectively. The XRD patterns for both the bare and the α-Fe_2O_3/Ox-Dex electrodes are shown in Fig. 1. Both electrodes presented the characteristic hematite peaks, described above in detail, while the peaks at 44° and 51° were assigned to the Cu from the electrode substrate.[51]

The morphological evaluation of the bare α-Fe_2O_3 electrode revealed the presence of macroscopic cracks, indicated with a white arrow (see Fig. 2a). However, such cracks were not observed for the hybrid electrodes (see Fig. 2b), which was attributed to the greater plasticity of the coating due to the presence of the polymeric material and its enhanced mechanical properties due to the favorable hydrogen bonding interactions between the hydroxyl functionalities of the hematite particles and the hydroxyl groups of Ox-Dex. For both electrodes, a tight packing of the cube-like particles was observed in higher magnification FE-SEM images (Fig. 2c and d). Finally, the presence of Ox-Dex was evidenced in the hybrid electrodes to form bridging linkages between the inorganic particles (highlighted with red arrows in Fig. 2f).

The wettability of the α-Fe_2O_3 and hybrid α-Fe_2O_3/Ox-Dex electrodes was then studied, and the water contact angle measurement results are shown in Fig. 3. An average water contact angle value of 30 ± 2° was found for the bare α-Fe_2O_3 electrode, indicating a hydrophilic surface (see Fig. 3a). The hydrophilicity stems from the strong cohesive forces between the water droplet and the hydroxyl groups present on the iron oxide surface.[52] Moreover, the hybrid α-Fe_2O_3/Ox-Dex electrode

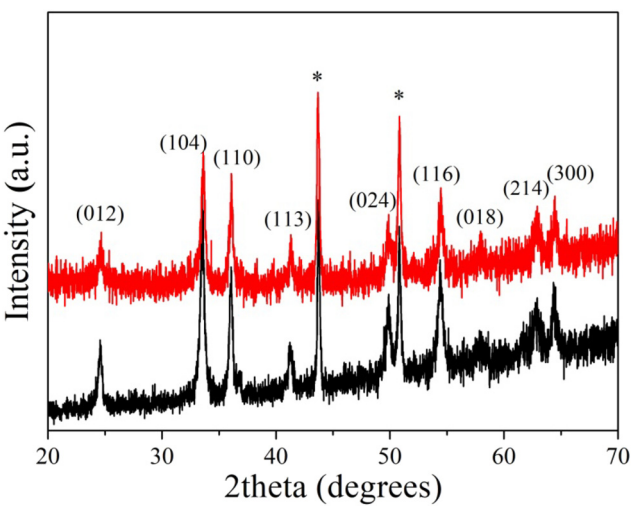

Fig. 1 XRD patterns of the bare α-Fe_2O_3 (black color) and the hybrid α-Fe_2O_3/Ox-Dex (red color) electrodes.

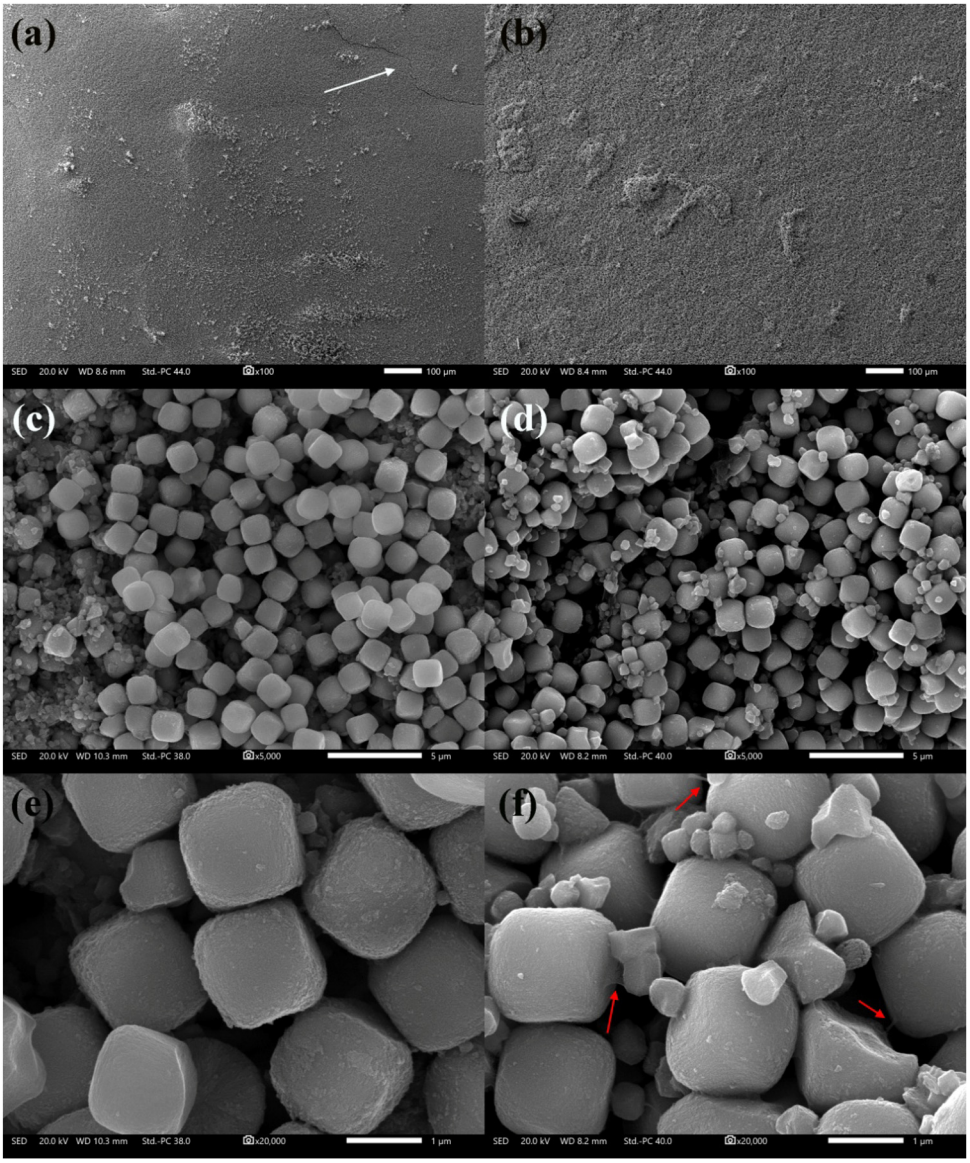

Fig. 2 FE-SEM images of the bare α-Fe_2O_3 (a, c and e) and the hybrid α-Fe_2O_3/Ox-Dex (b, d and f) electrodes at different magnifications.

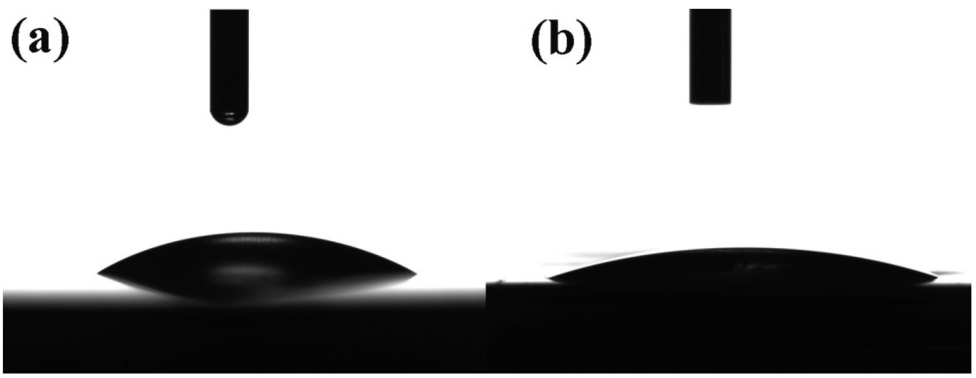

Fig. 3 Contact angle measurements on the surface of the bare α-Fe_2O_3 (a) and the hybrid α-Fe_2O_3/Ox-Dex (b) electrodes.

exhibited a nearly superhydrophilic behavior with a water contact angle of 19 ± 3°, due to the abundance of hydroxyl groups on the inorganic surface and on the polymer chains (see Fig. 3b).[53] This highly hydrophilic nature of the hybrid electrodes renders them attractive for use in aqueous electrolyte batteries, ensuring the good wetting of the electrode surface by the aqueous electrolyte solution.

3.3 Electrochemical evaluation of the electrodes

The electrochemical properties of the α-Fe_2O_3 and the hybrid α-Fe_2O_3/Ox-Dex electrodes were studied in 1 M Li_2SO_4 as a conventional Li-based electrolyte. Aqueous $ZnSO_4$ and $Al_2(SO_4)_3$ electrolyte solutions were also used to investigate the potential use of the electrodes in multivalent ion batteries.

3.3.1 Aqueous Li_2SO_4 electrolyte. The measurements were conducted over a potential range of −0.75 to +0.1 V in 1 M Li_2SO_4. The impact of the scan rate (0.005 to 0.1 V s^{-1}) on the redox behavior of the bare α-Fe_2O_3 electrode was examined (Fig. 4a). The CV curves consisted of a series of sharp and distinct cathodic (reduction) and anodic (oxidation) peaks centered at negative potential values. More specifically, the cathodic peak at −0.20 V corresponded to the reduction of α-$Li_2Fe_2O_3$ to produce Fe^0 and Li_2O (α-$Li_2Fe_2O_3$ + $4Li^+$ + $4e^-$ → $2Fe^0$ + $3Li_2O$) whereas the anodic peak at −0.17 V to the oxidation reaction of Fe^0 (Fe^0 → Fe^{3+}).[54] The strong anodic peak at around −0.56 V was assigned to the irreversible formation of a solid electrolyte interfacial (SEI) film and to side reactions between the electrode and the electrolyte.[55] It is noted that the SEI formation has stabilized, as indicated by the absence of a drop in the associated peak. The additional two redox peaks that appeared during the scans were attributed to the reduction of Cu^{2+} to Cu (cathodic process) and the oxidation of Cu to Cu^{2+} (anodic process).[56] The shape of the CV curve was similar for all scan rates demonstrating the reversibility of the redox processes,[57] while its non-rectangularity confirmed the pseudo-spatiality of the charge storage mechanisms.[58] The CV curves also showed that the peak separation increased when increasing the scan rate, with both the cathodic and anodic peaks being shifted to more positive and negative potentials, respectively. This change in the peak position was attributed to the polarization of the electrode.[59] The increase in the peak separation observed when increasing the scan rate signified the low resistance of the electrodes, which facilitates a rapid rate of ionic and electronic transport between the active material and the current collector.[60–62]

Furthermore, the anodic and cathodic maximum currents exhibited a linear dependence on the square root of the scan rate (see Fig. 4b). This suggests that the intercalation/de-intercalation process was controlled by the diffusion of the lithium ions in the host material.[63,64] The slopes of the linear depen-

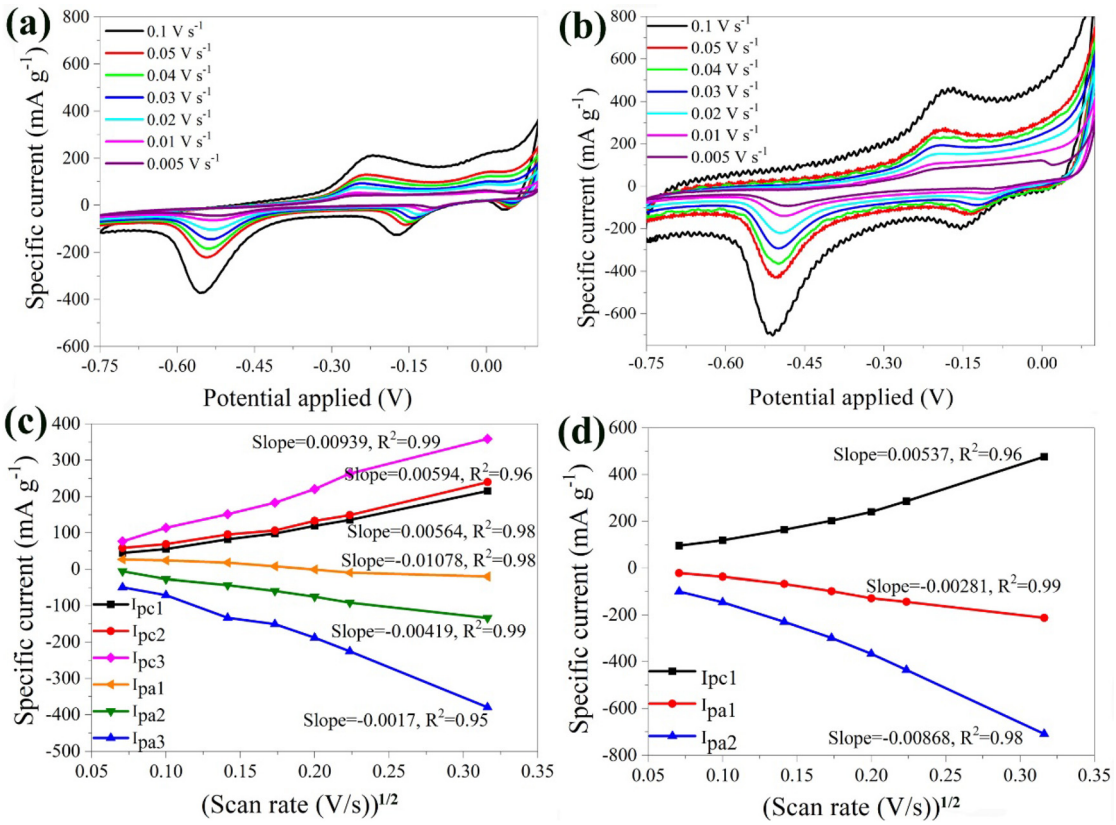

Fig. 4 Cyclic voltammograms of the bare α-Fe_2O_3 (a) and the hybrid α-Fe_2O_3/Ox-Dex (b) electrodes in 1 M Li_2SO_4 solution, recorded at different scan rates ranging from 0.005, 0.01, 0.02, 0.03, 0.04, 0.05 and 0.1 V s^{-1}. Cathodic and anodic maximum currents as a function of the square root of the scan rate for the bare α-Fe_2O_3 (c) and the hybrid α-Fe_2O_3/Ox-Dex (d) electrodes.

dencies of maximum current and the square root of the potential scan rates were analyzed using the Randles–Sevcik equation:[48]

$$I_{max} = 2.72 \times 10^5 \cdot n^{3/2} \cdot A \cdot C_{Li} \cdot D_{Li}{}^{1/2} \cdot V^{1/2}$$

where, I_{max}, n, A, V, D_{Li+}, C_{Li+} are the maximum current, number of exchanged electrons, submerged surface area of the electrode (0.75 × 1.5 cm^2), potential sweep rate, chemical diffusion coefficient of lithium ions and the concentration of lithium ions (*i.e.*, 1×10^{-3} mol cm^{-3}). The average value of D_{Li+} within the α-Fe_2O_3 framework was estimated ~7.01×10^{-11} cm^2 s^{-1}, which is within the range of the theoretical Li^+ diffusion value (*i.e.* 1.9×10^{-12} to 8×10^{-9} cm^2 s^{-1}).[65]

Fig. 4c shows the CV plots of the hybrid α-Fe_2O_3/Ox-Dex anode at different scan rates, ranging from 0.005 V s^{-1} to 0.1 V s^{-1}. The plots depicted a cathodic peak at −0.17 V and two anodic peaks at −0.15 V and −0.52 V. In particular, the first anodic peak around −0.17 V corresponded to the reduction of α-$Li_2Fe_2O_3$ to Fe^0 and Li_2O as discussed above for the α-Fe_2O_3 bare electrode.[66] The pronounced anodic peak at around −0.52 V was again attributed to the irreversible formation of the SEI film.[55] Regarding the cathodic peak at −0.17 V, it was associated with the oxidation of Fe^0. Interestingly, higher scan rates led to larger specific currents, reaching a maximum value of approximately 800 mA g^{-1} at a scan rate of 0.1 V s^{-1}. This suggested that the hybrid material exhibited a higher specific current compared to the bare α-Fe_2O_3 electrode, which was attributed to the hydrogen bonding interactions of the inorganic particles with the oxidized dextran binder, resulting in an increase of the contact points between the active materials.[67]

Moreover, the anodic and cathodic maximum currents demonstrated a linear dependence on the square root of the potential scan rate (Fig. 4d). The average value of D_{Li+} for the α-Fe_2O_3/Ox-Dex anode was found 2.69×10^{-10} cm^2 s^{-1}, higher than that of α-Fe_2O_3 (7.01×10^{-11} cm^2 s^{-1}). Consequently, a larger amount of Li^+ could be intercalated within the α-Fe_2O_3/Ox-Dex lattice, evidenced also by the higher specific current.

The stability of the bare α-Fe_2O_3 electrode was explored by varying the number of scans. A noticeable shift in the peaks was detected highlighting the possible instability of the material (Fig. 5a). This behavior was attributed to the loss of material in the electrolyte solution, caused by the electrolysis on the electrode surface and the oxidation of the Cu substrate by Li_2SO_4.[68] During electrolysis, positively charged ions migrate toward the cathode, while negatively charged ions move toward the anode. Prolonged electrolysis results in the accumulation of by-products on the electrode surface, and diminishes the electrochemical performance along with the lifespan of the electrode. The above were also visually evident by the presence of bubbles on the anode surface and the blue coloration of the electrolyte solution due to the oxidation of the Cu substrate (Fig. S3†).

Examination of the CV curves of the hybrid electrode at different scan rates (Fig. 5b) showed that the peaks of the first scan exhibited a lower specific current due to the required activation of the material. Subsequent scans, between 20 and 50, coincided, indicating an improved stability of the hybrid anode compared to the bare α-Fe_2O_3 electrode. This was further confirmed by calculating a variance percentage of 25.5% for the hybrid anode compared to 63% for the bare α-Fe_2O_3 electrode, derived by calculating the difference between the specific current recorded for the 100th scan and that of the 1st scan divided by the specific current of the 1st scan. The hybrid electrode's improved stability was due to the binder cross-linking ensuring superior structural integrity.[41] Most importantly, no material loss was observed in the electrolyte, verifying the excellent recyclability of the material.

3.3.2 Aqueous $ZnSO_4$ electrolyte. Experiments for the bare α-Fe_2O_3 electrode were also conducted using a 1 M aqueous $ZnSO_4$ electrolyte at a scan range of −0.65 to 0.15 V. The CV profiles measured at scan rates ranging from 0.005 to 0.1 V s^{-1}, revealed a distinct behavior of $ZnSO_4$ compared to Li_2SO_4. In this electrolyte, broad maxima were observed instead of sharp peaks, suggesting that the electrochemical processes may be either irreversible or quasi-reversible.[69] Irreversible processes occur when the oxidation or reduction reactions do

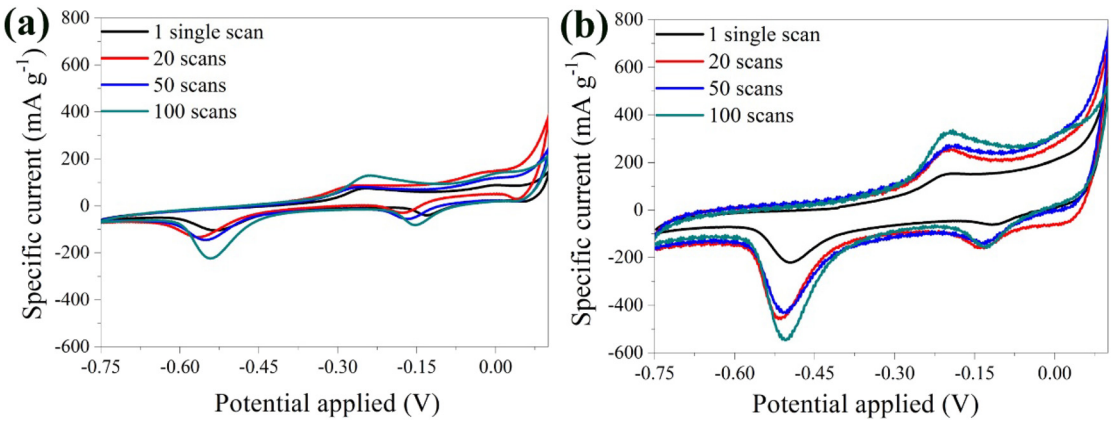

Fig. 5 CV curves of the bare α-Fe_2O_3 (a) and the hybrid α-Fe_2O_3/Ox-Dex (b) electrodes in 1 M Li_2SO_4 solution recorded at 1, 20, 50, 100 scans.

not easily reverse, possibly due to the slow electron transfer kinetics or strong adsorption of the Zn^{2+} ions onto the Fe_2O_3 matrix due to their higher charge and slightly smaller ionic radius compared to lithium ions.[70] The CV profile notably exhibited a cathodic maximum at +0.15 V and an anodic maximum at −0.65 V (Fig. 6a). The shape of the curves did not change, but the cathodic and anodic maxima gradually shifted to higher and lower values, attributed to the polarization effect discussed above for the Li_2SO_4 electrolyte. Moreover, the α-Fe_2O_3 electrode demonstrated a notable specific current of approximately 1200 mA g^{-1} at a scan rate of 0.1 V s^{-1}, far exceeding the 300 mA g^{-1} recorded for the Li^+ electrolyte. This increase was related to the divalent nature of zinc, which involves a greater number of electrons per ion in the electrochemical reaction, resulting in higher current.

Furthermore, the linear relationship between the maximum current and the square root of the scan rate confirmed that the reaction kinetics were diffusion-controlled (Fig. 6b). From the slope of the curve, the $D_{Zn^{2+}}$ for the α-Fe_2O_3 electrode was calculated and was found 3.62×10^{-10} cm^2 s^{-1}, surpassing the value of Li^+. This finding aligns with previous reports, which estimate the diffusion coefficients of Zn^{2+} between 10^{-11} – 10^{-10} cm^2 s^{-1}.[71] The smaller size of the zinc ions together with their larger charge, enhance their mobility within the active material's lattice compared to the lithium ions.[72]

Fig. 6c presents the CV plots of the hybrid α-Fe_2O_3/Ox-Dex electrode at different scan rates (0.005 V s^{-1} to 0.1 V s^{-1}) in a 1 M $ZnSO_4$ aqueous solution. The hybrid material exhibited a broad peak with maximum current in the anodic area, while a distinct peak was also observed in the cathodic region. This behavior suggests that the redox process may be irreversible. Notably, the maximum current increased as the scan rate approached 0.1 V s^{-1}, indicating a higher Zn^{2+} storage capacity.[73] Interestingly, these curves differ from those of the bare α-Fe_2O_3 electrode, since the peaks became more prominent at higher scan rates, suggesting that the presence of the polymer enhanced Zn ion diffusion. Furthermore, the anodic and cathodic maximum currents showed a linear relationship with the square root of the scan rate (Fig. 6d). The average $D_{Zn^{2+}}$ for the α-Fe_2O_3/Ox-Dex anode was 6.46×10^{-9} cm^2 s^{-1}, which is higher than that of the bare α-Fe_2O_3 electrode in the same electrolyte, in good agreement with the results discussed above for the Li_2SO_4 electrolyte. Most importantly, this value sets the record for the highest reported diffusion coefficient in aqueous electrolyte in the literature up to date,[74–78] apart from one reported very recently for Mo_6S_8.[79]

Fig. 7a shows the CV curves of the α-Fe_2O_3 electrode at a scan rate of 20 mV s^{-1} for the 1st, 20th, 50th, and 100th scans. An intense peak was observed in the first scan, followed by a gradual decrease in peak intensity in the subsequent scans, suggesting some material aging. Notably, for the 50th and

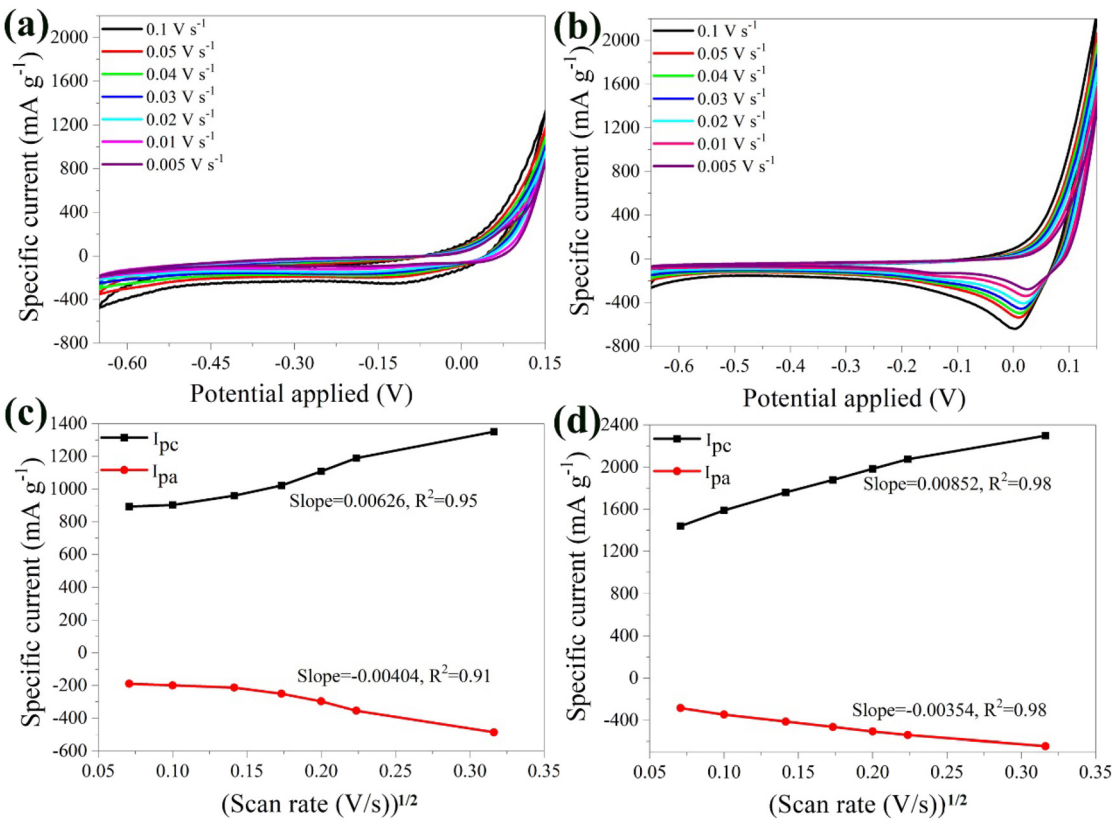

Fig. 6 CV curves of the bare α-Fe_2O_3 (a) and the hybrid α-Fe_2O_3/Ox-Dex (b) electrodes in 1 M $ZnSO_4$ solution recorded at different scan rates, 0.005, 0.01, 0.02, 0.03, 0.04, 0.05 and 0.1 V s^{-1}. The cathodic and anodic maximum currents as a function of the square root of the scan rate in 1 M $ZnSO_4$ for the bare α-Fe_2O_3 (c) and the hybrid α-Fe_2O_3/Ox-Dex (d) anodes.

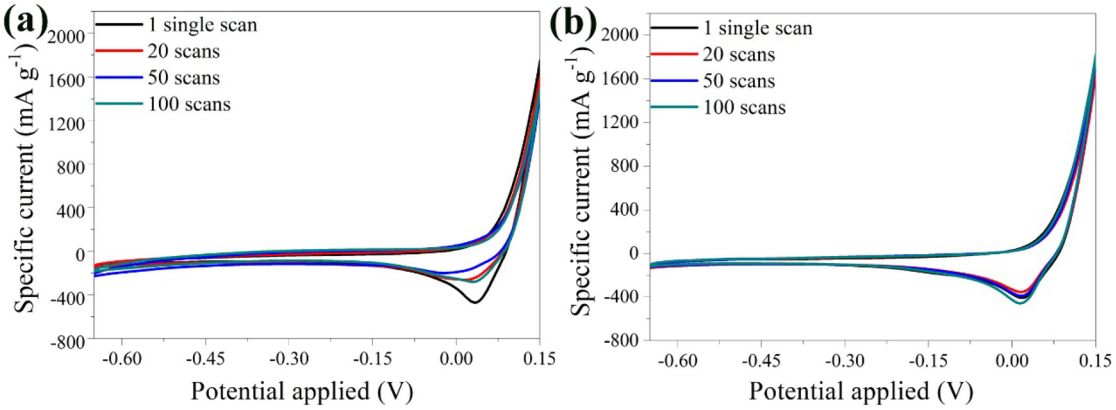

Fig. 7 CV curves of the bare α-Fe_2O_3 (a) and the hybrid α-Fe_2O_3/Ox-Dex (b) electrodes in 1 M $ZnSO_4$ electrolyte, recorded at 1, 20, 50, 100 scans.

100th scans, the curves nearly overlapped, indicating that the electrode remained stable and the variance percentage of bare electrode was estimated at 38.1%. In contrast, the CV curves for the hybrid material showed excellent electrochemical stability from the 1st to the 100th scan, with nearly complete overlap and a variance of just 1.3% between the 1st and the 100th scan (Fig. 7b). The peak position remained constant even for higher scan numbers, indicating a reversible phase transition during the Zn^{2+} intercalation/de-intercalation process.

Following 100 continuous intercalation/de-intercalation scans in the 1 M $ZnSO_4$ electrolyte, the hybrid α-Fe_2O_3/Ox-Dex electrode was characterized by FE-SEM and EDS. Small salt grains from the aqueous $ZnSO_4$ electrolyte were observed on the surface of the pseudocube-shaped particles, however, the hybrid electrodes maintained their integrity and structure (Fig. 8) due to the reasons discussed above. In addition, EDS analysis showed the presence of sulfur after 100 scans, attributed to the $ZnSO_4$ electrolyte on the hybrid electrode surface (Fig. S4†).

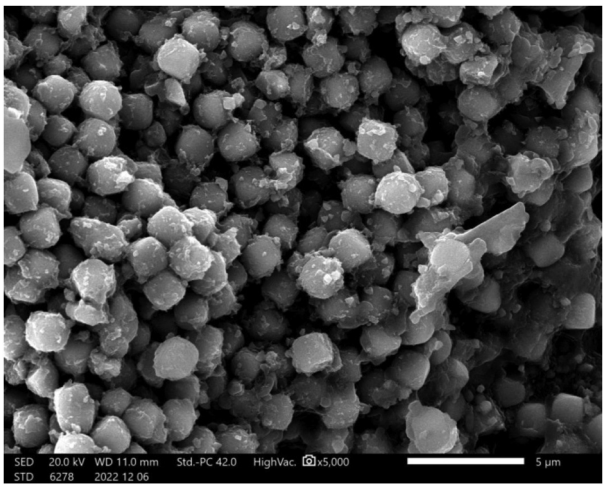

Fig. 8 FE-SEM image of the hybrid α-Fe_2O_3/Ox-Dex electrode after 100 continuous intercalation/de-intercalation scans in 1 M $ZnSO_4$ electrolyte solution.

3.3.3 Aqueous $Al_2(SO_4)_3$ electrolyte. The effect of scan rate on the redox behavior of the bare α-Fe_2O_3 electrode in an aqueous $Al_2(SO_4)_3{\cdot}H_2O$ electrolyte is shown in Fig. 9a. The CV curves at different scan rates, ranging from 0.005 to 0.1 V s^{-1}, showed one anodic peak at −0.05 V, and a distinct cathodic peak at +0.25 V, suggesting a similar reaction mechanism to $ZnSO_4$. The overall reaction mechanism between Fe_2O_3 and the aluminum cations, as the latter entered the iron oxide lattice, was determined by combining the oxidation and reduction half-reactions, ensuring equal electron transfer:[80]

$$Fe_2O_3 + 2Al \rightarrow Al_2O_3 + 2Fe + 3e^-$$

The anodic peak was shifted to lower potentials due to electrochemical polarization, with the effect being more pronounced for scan rates between 0.02 V s^{-1} and 0.05 V s^{-1}. Moreover, at 0.1 V s^{-1} strong noise was observed, likely caused by bubble formation on the anode. Despite the above, the bare α-Fe_2O_3 electrode exhibited a remarkable maximum specific current of 2000 mA g^{-1} at 0.1 V s^{-1}, the highest among all tested electrolytes (*i.e.* Li_2SO_4 (300 mA g^{-1}) and $ZnSO_4$ (1200 mA g^{-1})). This superior performance was attributed to the trivalent nature of the aluminum ions, resulting in stronger interactions with the anode. The smaller ionic size of the Al^{3+} cations (r = 68 pm) compared to Zn^{2+} (74 pm) and Li^+ (76 pm),[81] further enhanced ion mobility, leading to higher ionic conductivity.[10] Furthermore, the maximum current linear relationship with the square root of the scan rate revealed that the reaction kinetics were diffusion-controlled (Fig. 9b). The diffusion coefficient of the Al^{3+} cations for the bare α-Fe_2O_3 anode was calculated at 1.91 × 10^{-10} cm^2 s^{-1}, in good agreement with the values reported in the literature, which span from 10^{-11} cm^2 s^{-1} to 10^{-8} cm^2 s^{-1} under different conditions.[82–85]

Fig. 9c presents the CV plots for the hybrid α-Fe_2O_3/Ox-Dex electrode at scan rates ranging from 0.005 V s^{-1} to 0.1 V s^{-1}. Unlike the bare α-Fe_2O_3 anode, the hybrid material exhibited a maximum in the cathodic area at +0.25 V and an anodic peak at 0.00 V. The peak intensities increased with the scan rate, indicating an enhanced Al^{3+} storage capacity. The maximum specific

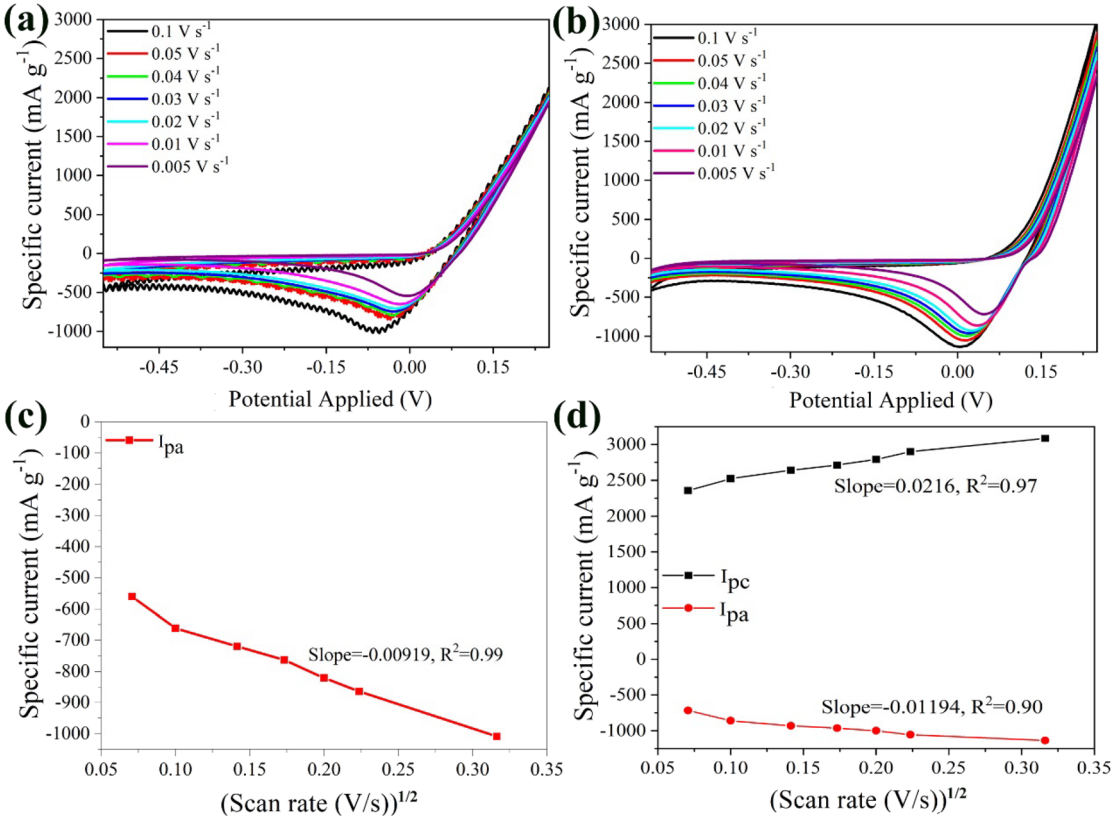

Fig. 9 CV curves of the bare α-Fe_2O_3 (a) and α-Fe_2O_3/Ox-Dex hybrid (b) electrodes in 1 M $Al_2(SO_4)_3$ solution recorded at different scan rates ranging from 0.005, 0.01, 0.02, 0.03, 0.04, 0.05 to 0.1 V s^{-1}. The cathodic and anodic maximum currents as a function of the square root of the scan rate in 1 M $Al_2(SO_4)_3$ electrolyte solution for the bare α-Fe_2O_3 (c) and the hybrid α-Fe_2O_3/Ox-Dex (d) anodes.

current was found 3000 mA g^{-1} at 0.1 V s^{-1}, surpassing that of the bare α-Fe_2O_3 electrode and all the other electrolytes studied in this work. In addition, the linear relationship between the anodic and cathodic maximum currents and the square root of the scan rate (Fig. 9d) allowed the calculation of $D_{Al^{3+}}$ for the α-Fe_2O_3/Ox-Dex anode, which was found 4.64 × 10^{-9} cm^2 s^{-1}. The higher diffusion coefficient suggests that trivalent aluminum ions entered more rapidly into the material's lattice. Once in the α-Fe_2O_3/Ox-Dex lattice, the Al^{3+} ions occupied three sites, thus increasing the number of available electrons and boosting the specific current. Additionally, the presence of cross-linked dextran improved electrode integrity, preventing material loss.

Fig. 10a shows the CV curves of the bare α-Fe_2O_3 electrode at 20 mV s^{-1} for the 1st, 20th, 50th and 100th scans.

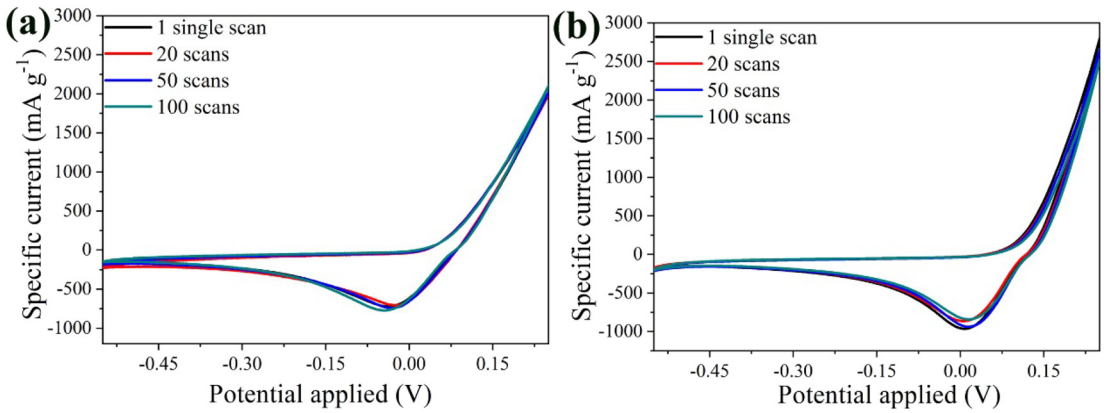

Fig. 10 CV curves for 1, 20, 50, and 100 scans for the bare α-Fe_2O_3 (a) and the hybrid α-Fe_2O_3/Ox-Dex (b) electrodes recorded in 1 M $Al_2(SO_4)_3$ electrolyte solution.

Remarkably, the overlapping curves from the 1st to the 100th scan highlight the excellent electrochemical stability of the anode. The constant peak position and curve shape indicated stable and reversible Al^{3+} intercalation/de-intercalation processes, supported by visual evidence of insignificant active material loss in the electrolyte during cycling. On the other hand, the performance of the hybrid electrode was superior to that of the bare α-Fe_2O_3 electrode after the 20th scan, despite a slight decrease in peak intensity after the 1st scan, attributed to minimal material aging (Fig. 10b). Specifically, the variance percentage was calculated 11.6% for α-Fe_2O_3 and 6.9% for α-Fe_2O_3/Ox-Dex, signifying an enhanced stability for the hybrid electrode.

4. Conclusions

In this study, sustainable and high-performance hybrid anode electrodes were designed, for applications in multivalent ion batteries. In-house synthesized hematite particles were chosen as the active anode material, while chemically modified dextran, a natural polysaccharide, was utilized as a cross-linkable binder, to immobilize the inorganic particles and enhance the stability of the hybrid electrodes. The design criteria of the proposed electrodes were based on the abundance, environmental friendliness, high chemical functionality, lack of toxicity, hydrophilicity and low cost of the chosen components. The bare and hybrid electrodes were evaluated in terms of their electrochemical performance in various aqueous electrolytes (including Li^+, Zn^{2+}, Al^{3+} ions), while particular emphasis was given to the ion diffusion mechanism and the stability of the material during multiple scans. The α-Fe_2O_3/Ox-Dex hybrid electrodes, tested in 1 M aqueous $ZnSO_4$, exhibited excellent electrochemical performance with a specific current of 2000 mA g^{-1} and good stability from the first scan, outperforming the bare α-Fe_2O_3 electrode (1200 mA g^{-1}). Similar electrochemical results were obtained for the hybrid electrode in 1 M aqueous $Al_2(SO_4)_3$ solution, which demonstrated a specific current of 3000 mA g^{-1} and stability up to the 20th scan compared to the bare α-Fe_2O_3 electrode (2000 mA g^{-1}). Finally, the calculated average diffusion coefficient value, $D_{Zn^{2+}}$, for the α-Fe_2O_3/Ox-Dex electrode was found exceptionally high at 6.46×10^{-9} cm^2 s^{-1}, one of the highest reported up to date. This remarkable diffusion rate was attributed to the divalent nature of the zinc ions, ensuring faster diffusion of the zinc cations compared to ions with smaller ionic radii. This accelerated diffusion allowed the zinc cations to enter the lattice of the active material more effectively, ensuring stability and minimizing fragmentation of the anode electrode. The pronounced electrochemical performance and stability observed for the α-Fe_2O_3/Ox-Dex hybrid anodes compared to the α-Fe_2O_3 analogues were assigned to hydrogen bonding interactions between the functional groups of the two materials. Moreover, these favorable chemical interactions enhanced the specific current and the resistance to volume expansion during the intercalation/de-intercalation processes. Future work will delve into optimizing the fabrication process, exploring additional environmentally friendly components and current collectors such as Ni and stainless steel, and conducting comprehensive assessments under diverse operating conditions for longer scans aiming to advance the understanding of the role of hybrid materials in energy storage systems and to enhance their practical viability in real applications.

Data availability

The data supporting the findings of this study can be found in this article or in the ESI.†

Conflicts of interest

The authors declare that there are no conflicts of interest.

Acknowledgements

This research was funded by the European Union through the Twinning project FORGREENSOFT (Number: 101078989 under HORIZON-WIDERA-2021-ACCESS-03).

References

1 A. Tomaszewska, Z. Chu, X. Feng, S. O'Kane, X. Liu, J. Chen, C. Ji, E. Endler, R. Li, L. Liu, Y. Li, S. Zheng, S. Vetterlein, M. Gao, J. Du, M. Parkes, M. Ouyang, M. Marinescu, G. Offer and B. Wu, *eTransportation*, 2019, **1**, 100011.
2 Y. Chen, Y. Kang, Y. Zhao, L. Wang, J. Liu, Y. Li, Z. Liang, X. He, X. Li, N. Tavajohi and B. Li, *J. Energy Chem.*, 2021, **59**, 83–99.
3 M. A. Schroeder, L. Ma, G. Pastel and K. Xu, *Curr. Opin. Electrochem.*, 2021, **29**, 100819.
4 Y. Liu, L. Kang, X. Lu, P. R. Shearing, W. Ahmed, G. He and D. J. L. Brett, in *Micro and Nano Technologies*, ed. R. K. Gupta, T. A. Nguyen and S. Yasin, Elsevier, 2022, pp. 315–340.
5 X. Li, Y. Tang, H. Lv, W. Wang, F. Mo, G. Liang, C. Zhi and H. Li, *Nanoscale*, 2019, **11**, 17992–18008.
6 C. Xu, B. Li, H. Du and F. Kang, *Angew. Chem., Int. Ed.*, 2012, **51**, 933–935.
7 J. Ming, J. Guo, C. Xia, W. Wang and H. N. Alshareef, *Mater. Sci. Eng., R*, 2019, **135**, 58–84.
8 S. Kang, K. G. Reeves, T. Koketsu, J. Ma, O. J. Borkiewicz, P. Strasser, A. Ponrouch and D. Dambournet, *ACS Appl. Energy Mater.*, 2020, **3**, 9143–9150.
9 G. A. Elia, K. V. Kravchyk, M. V. Kovalenko, J. Chacón, A. Holland and R. G. A. Wills, *J. Power Sources*, 2021, **481**, 228870.
10 T. Leisegang, F. Meutzner, M. Zschornak, W. Münchgesang, R. Schmid, T. Nestler, R. A. Eremin,

A. A. Kabanov, V. A. Blatov and D. C. Meyer, *Front. Chem.*, 2019, **7**, 1–21.
11 H. Wang, S. Chen, C. Fu, Y. Ding, G. Liu, Y. Cao and Z. Chen, *ACS Mater. Lett.*, 2021, **3**, 956–977.
12 S. Liu, J. J. Hu, N. F. Yan, G. L. Pan, G. R. Li and X. P. Gao, *Energy Environ. Sci.*, 2012, **5**, 9743–9746.
13 Y. Liang, H. Dong, D. Aurbach and Y. Yao, *Nat. Energy*, 2020, **5**, 646–656.
14 Y. Zhang, X. Zheng, N. Wang, W.-H. Lai, Y. Liu, S.-L. Chou, H.-K. Liu, S.-X. Dou and Y.-X. Wang, *Chem. Sci.*, 2022, **13**, 14246–14263.
15 J. Meng, X. Yao, X. Hong, L. Zhu, Z. Xiao, Y. Jia, F. Liu, H. Song, Y. Zhao and Q. Pang, *Nat. Commun.*, 2023, **14**, 3909.
16 S. Goriparti, E. Miele, F. De Angelis, E. Di Fabrizio, R. Proietti Zaccaria and C. Capiglia, *J. Power Sources*, 2014, **257**, 421–443.
17 P. Roy and S. K. Srivastava, *J. Mater. Chem. A*, 2015, **3**, 2454–2484.
18 J. Chen and F. Cheng, *Acc. Chem. Res.*, 2009, **42**, 713–723.
19 P. Kumar, K.-H. Kim, V. Bansal and P. Kumar, *Coord. Chem. Rev.*, 2017, **353**, 113–141.
20 L. S. Roselin, R. S. Juang, C. T. Hsieh, S. Sagadevan, A. Umar, R. Selvin and H. H. Hegazy, *Materials*, 2019, **12**, 1229.
21 H. Mou, W. Xiao, C. Miao, R. Li and L. Yu, *Front. Chem.*, 2020, **8**, 1–14.
22 R. Amine, A. Daali, X. Zhou, X. Liu, Y. Liu, Y. Ren, X. Zhang, L. Zhu, S. Al-Hallaj, Z. Chen, G. L. Xu and K. Amine, *Nano Energy*, 2020, **74**, 104849.
23 H. Shi, C. Shi, Z. Jia, L. Zhang, H. Wang and J. Chen, *RSC Adv.*, 2022, **12**, 33641–33652.
24 S. Fang, D. Bresser and S. Passerini, *Adv. Energy Mater.*, 2020, **10**, 1902485.
25 S. Lou, Y. Zhao, J. Wang, G. Yin, C. Du and X. Sun, *Small*, 2019, **15**, 1–44.
26 X. Zheng and J. Li, *Ionics*, 2014, **20**, 1651–1663.
27 L. Zhang, H. Bin Wu and X. W. Lou, *Adv. Energy Mater.*, 2014, **4**, 1–11.
28 Y. M. Lin, P. R. Abel, A. Heller and C. B. Mullins, *J. Phys. Chem. Lett.*, 2011, **2**, 2885–2891.
29 D. Guy, B. Lestriez, R. Bouchet and D. Guyomard, *J. Electrochem. Soc.*, 2006, **153**, A679.
30 J. Yoon, J. Lee, H. Kim, J. Kim and H.-J. Jin, *Polymers*, 2024, **16**, 254.
31 R. R. Li, Z. Yang, X. X. He, X. H. Liu, H. Zhang, Y. Gao, Y. Qiao, L. Li and S. L. Chou, *Chem. Commun.*, 2021, **57**, 12406–12416.
32 S. Lee, H. Koo, H. S. Kang, K.-H. Oh and K. W. Nam, *Polymers*, 2023, **15**, 4477.
33 Y. Yang, S. Wu, Y. Zhang, C. Liu, X. Wei, D. Luo and Z. Lin, *Chem. Eng. J.*, 2021, **406**, 126807.
34 H. Zheng, L. Ma, P. Yi, Z. Fang, Y. Yuan, J. Shen and M. Ye, *Nanoscale*, 2024, **16**, 20765–20773.
35 W. Dou, M. Zheng, W. Zhang, T. Liu, F. Wang, G. Wan, Y. Liu and X. Tao, *Adv. Funct. Mater.*, 2023, **33**, 2305161.
36 D. Bresser, D. Buchholz, A. Moretti, A. Varzi and S. Passerini, *Energy Environ. Sci.*, 2018, **11**, 3096–3127.
37 N. Lingappan, L. Kong and M. Pecht, *Renewable Sustainable Energy Rev.*, 2021, **147**, 111227.
38 Y. K. Jeong, T. Kwon, I. Lee, T.-S. Kim, A. Coskun and J. W. Choi, *Nano Lett.*, 2014, **14**, 864–870.
39 M. T. Jeena, J.-I. Lee, S. H. Kim, C. Kim, J.-Y. Kim, S. Park and J.-H. Ryu, *ACS Appl. Mater. Interfaces*, 2014, **6**, 18001–18007.
40 M. Ling, J. Qiu, S. Li, C. Yan, M. J. Kiefel, G. Liu and S. Zhang, *Nano Lett.*, 2015, **15**, 4440–4447.
41 X. Zhao, C. H. Yim, N. Du and Y. Abu-Lebdeh, *Ind. Eng. Chem. Res.*, 2018, **57**, 9062–9074.
42 Z. Li, S. Gu, K. Liao, H. Wang, L. Yin, Y. Cao, N. Qin, Q. Gan, Y. Li, Z. Wang, S. Yin and Z. Lu, *Mater. Today Energy*, 2023, **34**, 101298.
43 H. Ahn, D. Kim, M. Lee and K. W. Nam, *Commun. Mater.*, 2023, **4**, 1–19.
44 T. Sugimoto, M. M. Khan and A. Muramatsu, *Colloids Surf., A*, 1993, **70**, 167–169.
45 A. Jeanes and C. A. Wilham, *J. Am. Chem. Soc.*, 1950, **72**, 2655–2657.
46 H. Zhao and N. D. Heindel, *Pharm. Res.*, 1991, **8**, 400–402.
47 M. Panagopoulou, D. Vernardou, E. Koudoumas, D. Tsoukalas and Y. S. Raptis, *Electrochim. Acta*, 2019, **321**, 134743.
48 S. Daskalakis, M. Wang, C. J. Carmalt and D. Vernardou, *Nanomaterials*, 2021, **11**, 1–8.
49 J. M. Meijer and L. Rossi, *Soft Matter*, 2021, **17**, 2354–2368.
50 M. Niederberger, F. Krumeich, K. Hegetschweiler and R. Nesper, *Chem. Mater.*, 2002, **14**, 78–82.
51 M. Eslami, F. Golestani-fard, H. Saghafian and A. Robin, *Mater. Des.*, 2014, **58**, 557–569.
52 K. Tang, X. Lv, S. Wu, S. Xuan, X. Huang and C. Bai, *ISIJ Int.*, 2018, **58**, 379–400.
53 S. Martwiset, A. E. Koh and W. Chen, *Langmuir*, 2006, **22**, 8192–8196.
54 J. Luo, X. Xia, Y. Luo, C. Guan, J. Liu, X. Qi, C. F. Ng, T. Yu, H. Zhang and H. J. Fan, *Adv. Energy Mater.*, 2013, **3**, 737–743.
55 Y. Xiang, Z. Yang, S. Wang, M. S. A. Hossain, J. Yu, N. A. Kumar and Y. Yamauchi, *Nanoscale*, 2018, **10**, 18010–18018.
56 A. Jaikumar, K. S. V. Santhanam, S. G. Kandlikar, I. B. P. Raya and P. Raghupathi, *ECS Trans.*, 2015, **66**, 55.
57 J. Zhou, S. Xu, L. Ni, N. Chen, X. Li, C. Lu, X. Wang, L. Peng, X. Guo, W. Ding and W. Hou, *J. Power Sources*, 2019, **438**, 227047.
58 C. Costentin and J. M. Savéant, *Chem. Sci.*, 2019, **10**, 5656–5666.
59 Y. Guo, X. Li, H. Guo, Q. Qin, Z. Wang, J. Wang and G. Yan, *Energy Storage Mater.*, 2022, **51**, 476–485.
60 P. Rangaswamy, G. S. Suresh and M. M. Kittappa, *J. Solid State Electrochem.*, 2016, **20**, 2619–2631.
61 G. J. Wang, Q. T. Qu, B. Wang, Y. Shi, S. Tian, Y. P. Wu and R. Holze, *Electrochim. Acta*, 2009, **54**, 1199–1203.

62 S. Siracusano, V. Baglio, N. Van Dijk, L. Merlo and A. S. Aricò, *Appl. Energy*, 2017, **192**, 477–489.
63 L. Xu, Y. Tian, T. Liu, H. Li, J. Qiu, S. Li, H. Li, S. Yuan and S. Zhang, *Green Energy Environ.*, 2018, **3**, 156–162.
64 C. Floraki, M. Androulidaki, E. Spanakis and D. Vernardou, *Nanomaterials*, 2023, **13**, 1850.
65 J. M. Lee, G. Singh, W. Cha, S. Kim, J. Yi, S. J. Hwang and A. Vinu, *ACS Energy Lett.*, 2020, **5**, 1939–1966.
66 X. Liu, W. Si, J. Zhang, X. Sun, J. Deng, S. Baunack, S. Oswald, L. Liu, C. Yan and O. G. Schmidt, *Sci. Rep.*, 2014, **4**, 1–8.
67 T. Qin, H. Yang, Q. Li, X. Yu and H. Li, *Ind. Chem. Mater.*, 2024, **2**, 191–225.
68 K. Lota, P. Swoboda, I. Acznik, A. Sierczyńska, R. Mańczak, Ł. Kolanowski and G. Lota, *Curr. Appl. Phys.*, 2020, **20**, 106–113.
69 Z. Li and A. W. Robertson, *Battery Energy*, 2023, **2**, 20220029.
70 Y. Shang and D. Kundu, *Batteries Supercaps*, 2022, **5**, e202100394.
71 N. Zhang, Y. Dong, M. Jia, X. Bian, Y. Wang, M. Qiu, J. Xu, Y. Liu, L. Jiao and F. Cheng, *ACS Energy Lett.*, 2018, **3**, 1366–1372.
72 Y. Tan, F. An, Y. Liu, S. Li, P. He, N. Zhang, P. Li and X. Qu, *J. Power Sources*, 2021, **492**, 229655.
73 C. Xie, Y. Li, Q. Wang, D. Sun, Y. Tang and H. Wang, *Carbon Energy*, 2020, **2**, 540–560.
74 L. Wang, J. Zou, S. Chen, G. Zhou, J. Bai, P. Gao, Y. Wang, X. Yu, J. Li, Y.-S. Hu and H. Li, *Energy Storage Mater.*, 2018, **12**, 216–222.
75 L. Wen, Y. Wu, S. Wang, J. Shi, Q. Zhang, B. Zhao, Q. Wang, C. Zhu, Z. Liu, Y. Zheng, J. Su and Y. Gao, *Nano Energy*, 2022, **93**, 106896.
76 B. Lee, H. R. Lee, H. Kim, K. Y. Chung, B. W. Cho and S. H. Oh, *Chem. Commun.*, 2015, **51**, 9265–9268.
77 N. Zhang, M. Jia, Y. Dong, Y. Wang, J. Xu, Y. Liu, L. Jiao and F. Cheng, *Adv. Funct. Mater.*, 2019, **29**, 1807331.
78 E. Levi, G. Gershinsky, D. Aurbach, O. Isnard and G. Ceder, *Chem. Mater.*, 2009, **21**, 1390–1399.
79 A. Elgendy, A. A. Papaderakis, A. Ejigu, K. Helmbrecht, B. F. Spencer, A. Groß, A. S. Walton, D. J. Lewis and R. A. W. Dryfe, *Nanoscale*, 2024, **16**, 13597–13612.
80 Y. Wang, X. Song, W. Jiang, G. Deng, X. Guo, H. Liu and F. Li, *Trans. Nonferrous Met. Soc. China*, 2014, **24**, 263–270.
81 G. A. Elia, K. Marquardt, K. Hoeppner, S. Fantini, R. Lin, E. Knipping, W. Peters, J. F. Drillet, S. Passerini and R. Hahn, *Adv. Mater.*, 2016, **28**, 7564–7579.
82 K. L. Ng, B. Amrithraj and G. Azimi, *Joule*, 2022, **6**, 134–170.
83 M. Kazazi, P. Abdollahi and M. Mirzaei-Moghadam, *Solid State Ionics*, 2017, **300**, 32–37.
84 J. Tu, M. Wang, X. Xiao, H. Lei and S. Jiao, *ACS Sustainable Chem. Eng.*, 2019, **7**, 6004–6012.
85 W. Tang, J. Xuan, H. Wang, S. Zhao and H. Liu, *J. Power Sources*, 2018, **384**, 249–255.